applied sciences

MDPI

Article

Volume Contraction in Shallow Sediments: Discrete Element Simulation

Minsu Cha [1,*] and J. Carlos Santamarina [2]

[1] Department of Civil Engineering, Jeju National University, Jeju-si 63243, Korea
[2] Earth Science and Engineering, King Abdullah University of Science and Technology KAUST, Thuwal 23955-6900, Saudi Arabia
* Correspondence: mcha@office.jejunu.ac.kr

Abstract: Displacements induced by mineral dissolution and subsurface volume contraction affect overlying soils. In this study, we examine the consequences of mass loss or volume contraction at shallow depths using a discrete element method. The goal of the study is to identify particle-scale and global effects as a function of the relative depth of a dissolving inclusion, initial soil density, and granular interlocking. There are successive arch formation and collapse events, and a porosity front propagates upwards as grains slide down to refill the space. Grains around and within the refilled cavity are loosely packed and have small contact forces that are sufficient to avert the buckling of granular arches that form around the dissolving zone. Denser packings and interlocking combine to exacerbate rotational frustration and lead to more pronounced force chains along granular arches, looser fill, and reduced surface settlement. In fact, surface settlement vanishes, and the sediment hides the localized dissolution when deep inclusions $z/D \geq 5$ dissolve within dense sediments. While scaling relations limit the extrapolation of these numerical results to tunneling and mining applications, macroscale trends observed in the field resemble results gathered in this study.

Keywords: subsurface volume contraction; mineral dissolution; granular arching; surface settlement; internal grain displacement; discrete element method

Citation: Cha, M.; Santamarina, J.C. Volume Contraction in Shallow Sediments: Discrete Element Simulation. *Appl. Sci.* **2022**, *12*, 8015. https://doi.org/10.3390/app12168015

Academic Editor: Arcady Dyskin

Received: 9 June 2022
Accepted: 9 August 2022
Published: 10 August 2022

1. Introduction

Mineral dissolution and precipitation are concurrent soil processes. The time scale for chemical processes is typically quite long and the "inert assumption of soils" applies to many engineering applications. Dissolution and precipitation, however, can also take place in relatively short time scales in advective regimes and when systems are taken far from equilibrium. They occur, for example, in dam foundations, volcanic ash, mine tailings, fly ash, CO_2 injection, infiltration-induced carbonate dissolution, and the dissociation of segregated ice or methane hydrates [1–7].

Volume contraction in shallow sediments can take place during mining operations and due to ground loss around underground construction [8–11]. Similarly, the localized dissolution of carbonates may trigger ground subsidence, cave-ins and regional softening [12,13]. Ensuing subsidence, collapse and sinkholes are a function of soil properties, volume loss and geometry (size, depth). Displacements induced by underground volume contraction negatively affect the overlying infrastructure and nearby underground structures. As examples, piles experience lateral deflection, bending moments, settlement, and abnormal load distribution [14–17]; lifelines are sheared and disrupted [18–21]; buildings develop differential settlement and horizontal displacement [22–24]; and adjacent tunnels may rotate and undergo asymmetric settlement [25,26].

Previous studies of mineral dissolution and subsurface volume contraction using the discrete element method have primarily addressed pressure solution [27–29], randomly distributed soluble grains [30] and volume loss around tunnels [31,32]. This study takes

advantage of the discrete element method to obtain macroscale and particle-level information following the dissolution of a granular inclusion at shallow depth. Variables include sediment density and granular interlocking, and the inclusion depth.

2. Methodology

We use the two-dimensional discrete element code PFC-2D (ITASCA Consulting Group, Inc.) to create the simulation environment (details in Table 1). The grain size distribution is uniform and ranges between d_{min} = 0.8 mm and d_{max} = 1.2 mm; the uniform size distribution is selected to avoid computational instability caused by very small particles generated in a normal distribution and to avoid preferential particle aligning along boundaries in mono-sized particles. We select the linear grain contact model, the available model in PFC2D for 2D disks [33], and apply an interparticle friction of 0.5, a typical value used in the literature to produce a reasonable macro-scale friction angle of granular soils [34]. We impose no friction between grains and walls, a common boundary assumption adopted to simulate field conditions in a cell environment.

Table 1. Two-dimensional discrete element simulation environment.

	Properties	Values
Particles (disks)	Diameter	Uniform size distribution (d_{min} = 0.8 mm, d_{max} = 1.2 mm)
	Number of disks	10,567
	Density of disks	2650 kg/m^3
	Linear contact model	Normal stiffness $k_n = 10^8$ N/m
		Shear stiffness $k_s = 10^8$ N/m
	Inter-particle friction	0.5
	Local damping	0.7
Inclusion	Diameter	D = 10 mm
Boundary conditions	Initial cell size	100 mm × 100 mm
	Free upper surface	
	Rigid, zero lateral strain	
	Particle-to-wall friction	0
	Gravity	1 g

Grain angularity and interlocking, which imply rotational resistance, can be numerically implemented by imposing rolling resistance [35–38] or by introducing non-spherical particles and granular clusters [39–41]. Hindered particle rotation (HR) is a computationally efficient approach to account for grain angularity [42,43]. Numerical results are physically inconsistent when all particles have hindered rotation; in this study, we hinder the rotation of an HR-fraction of randomly located particles. Numerical simulations show that the macroscale friction angle increases with interlocking: $\phi = 22^\circ$ for HR = 0%, $\phi = 35^\circ$ for HR = 40%, and $\phi = 48^\circ$ for HR = 80% [44].

We create normally compacted granular assemblies ("clean sand") with two markedly different initial densities. The loose packing is formed by air pluviation, in which particles are poured from a low height, gradually filling the container bottom-up under 1 g gravity. We form the dense packing by loading granular packing with zero interparticle friction and no gravity; then, we reinstate friction and gravity after unloading. Finally, we select particles with hindered rotation at random before dissolution starts.

The dissolvable granular inclusion has a D = 10 mm diameter and is buried at various depths z (Figure 1). The vertical walls impose zero-lateral deformation, and the upper

sediment surface is stress-free. Altogether, we run 18 cases to explore loose (e = 0.242) and dense (e = 0.184) initial packings, three burial depths (z/D = 2, 5, and 9), and three levels of granular interlocking (HR = 0%, 40%, and 80%) to vary the macroscopic friction angle.

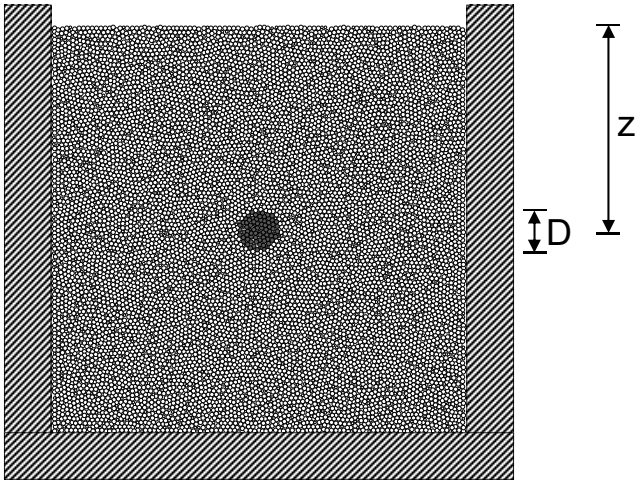

Figure 1. Initial model showing inclusion depth z and size D. Dark-colored grains are soluble. (This case corresponds to z/D = 5).

We simulate subsurface volume contraction by removing the granular inclusion. We test two dissolution modes: quasi-static gradual grain contraction (each run requires several weeks to keep the inertia number $I < 10^{-5}$) and instantaneous removal of the grains (each run requires only a day, but inertia arises in early particle flow). In both cases, the final sediment conditions are very similar (Figure 2). All results reported next are obtained by instantaneous removal.

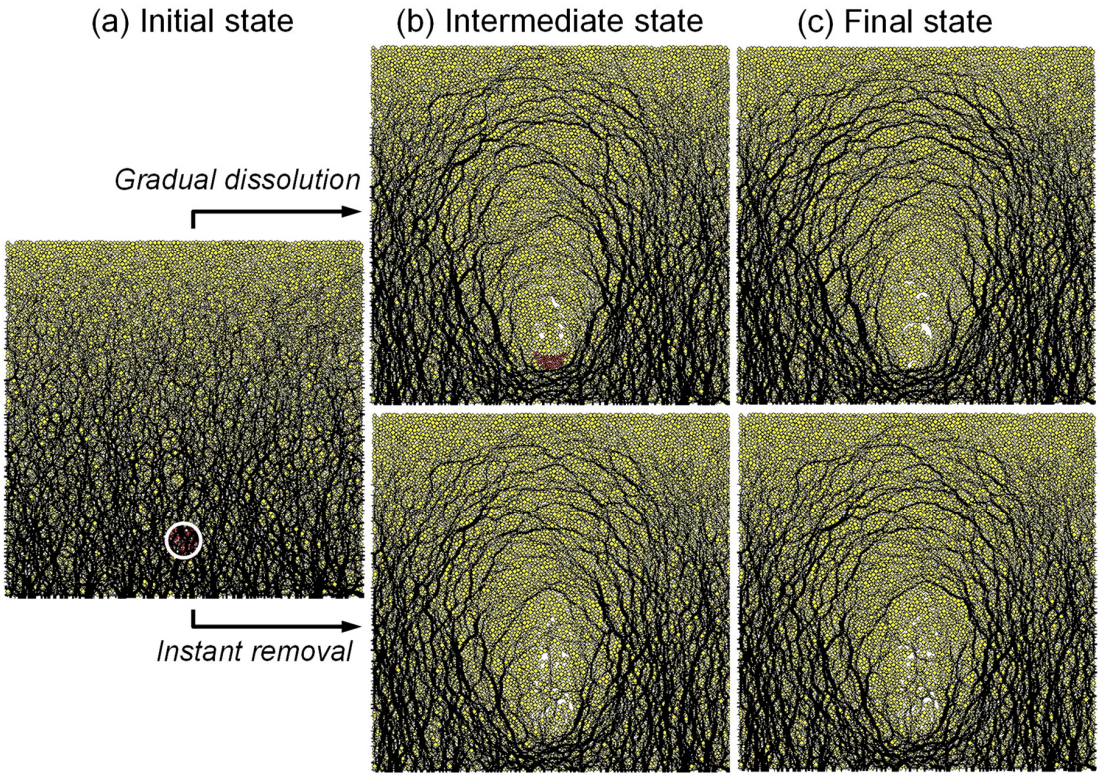

Figure 2. Force chains during subsurface volume contraction: quasi-static gradual dissolution vs. instantaneous removal. The white circle indicates the original location of dissolvable inclusions, and

the red particles are soluble. (**a**) Initial force chains. (**b**) Intermediate state during dissolution or after instantaneous removal. (**c**) Final force chains. Note: medium dense packing (e = 0.201), HR = 80%, z/D = 8.5.

3. Results and Analyses

Grain flow. Grain flow is accompanied by successive arch formation and collapse events. Grains slide and flow predominantly in the vertical direction to refill the cavity and a counter-propagating porosity front emerges (Figure 3). The flow stream is narrower in sediments with higher interlocking (Figure 3; full dataset in Figure S1 of the Supplementary Data).

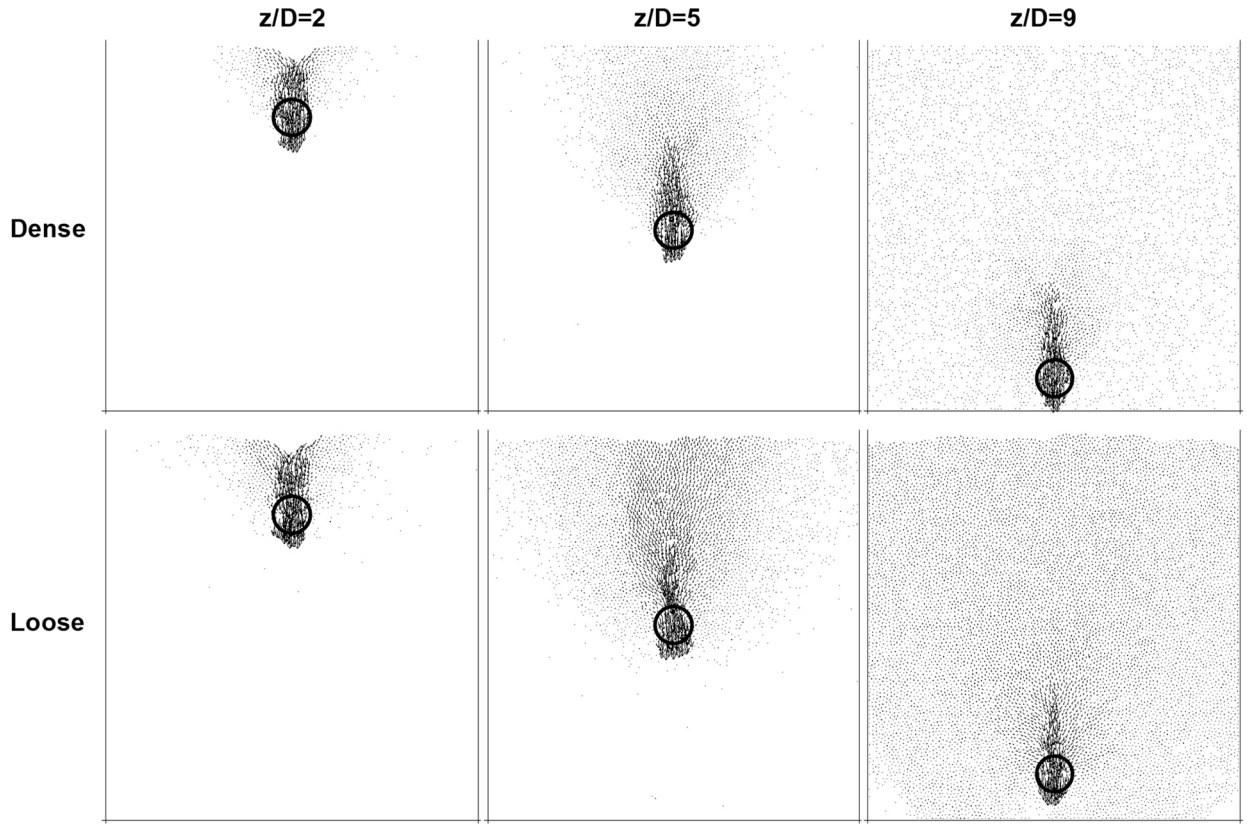

Figure 3. Granular flow during cavity refill—displacement vectors. Vector magnitudes are equally scaled for all cases. The black circles indicate the original location and size of the dissolving inclusions. Note: hindered rotation HR = 40%.

Contact force arching and refilled cavity. Grains in the refilled cavity are loosely packed; the small forces they carry provide transverse support to the granular arches that form around the dissolving zone (see Figure 4 and the complete dataset in Figure S2 of the Supplementary Data). In terms of contact forces, a "ghost zone" remains after dissolution and it extends beyond the original inclusion size. The egg-shaped force arches extend towards the free surface and define more prominent ghost zones in cases that involve deeper dissolution, denser sediments and higher interlocking. Clearly, rotational frustration plays an important role in particle rearrangement; thus, a higher coordination number in denser packings and hindered rotation combine to exacerbate rotational frustration, marked force chains and loose refill.

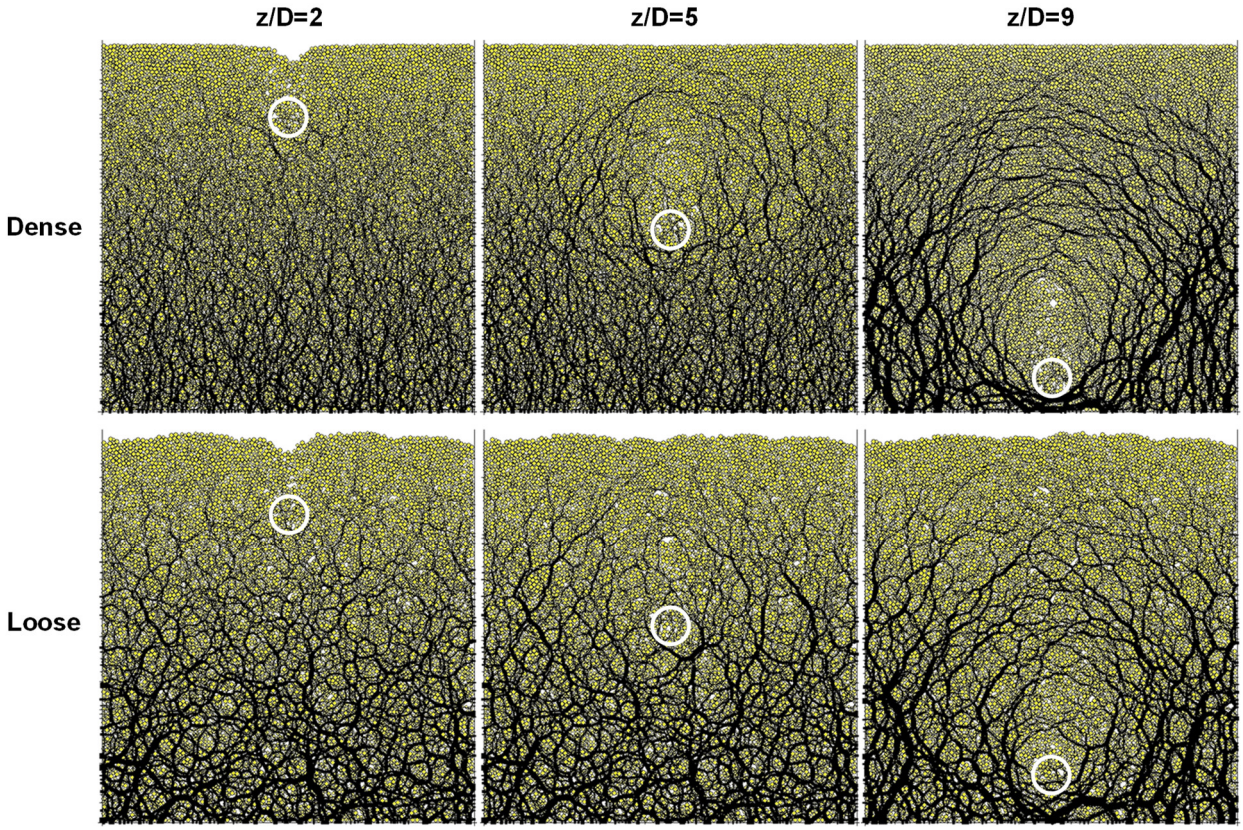

Figure 4. Contact force chains after dissolution. Force chain thicknesses reflect the force magnitude and are equally scaled for all cases. The white circles indicate the original location of dissolvable inclusions. Notice large local porosity next to strong force chains. Case: hindered rotation HR = 40%.

Settlement. Figure 5 summarizes surface settlement profiles for all 18 cases. We fit a Gaussian function to each dataset to extract the maximum surface settlement δ_{max} and the "characteristic width" W of the settlement trough. This analysis resembles large-scale field observations of previous studies [12,45–47]:

$$\delta_x = \delta_{max} \exp\left(-\frac{x^2}{2\Sigma^2}\right), \quad (1)$$

where x is the horizontal distance from the centerline and Σ the standard deviation. Maximum surface settlement δ_{max} decreases as the depth–size ratio z/D increases. Interlocking and packing density (1) do not affect δ_{max} for very shallow inclusions $z/D \leq 2$, where surface settlement is kinematically controlled, but (2) reduce the peak settlement δ_{max} when inclusions are deeper than $z/D \geq 5$ and granular flow is equilibrium-controlled (Figures 5 and 6a). In all cases, effective width Σ increases as z/D increases and interlocking decreases.

Trough area vs. *lost area*. Simulation results allow us to compare the trough area A_{tr} against the area of contracting zone A_{cz}. In most cases, the ratio is $A_{tr}/A_{cz} < 1$. In fact, surface settlement vanishes, and $A_{tr}/A_{cz} \rightarrow 0$ for deep cavities $z/D \geq 5$ dissolving in dense sediments with high interlocking (Figure 6b). In the limit of incompressible grains, difference $A_{cz} - A_{tr}$ is equal to the gain in internal voids and porosity, as can be seen in the numerical results (Figure 2, Figure 4 and Figure S2). Note that the trough area exceeds the area of the dissolved inclusion $A_{tr}/A_{cz} > 1$ when dissolution takes place in loose sediments with no rotational resistance; in this case, dissolution triggers the densification of the overlying sediment (Figure 6b).

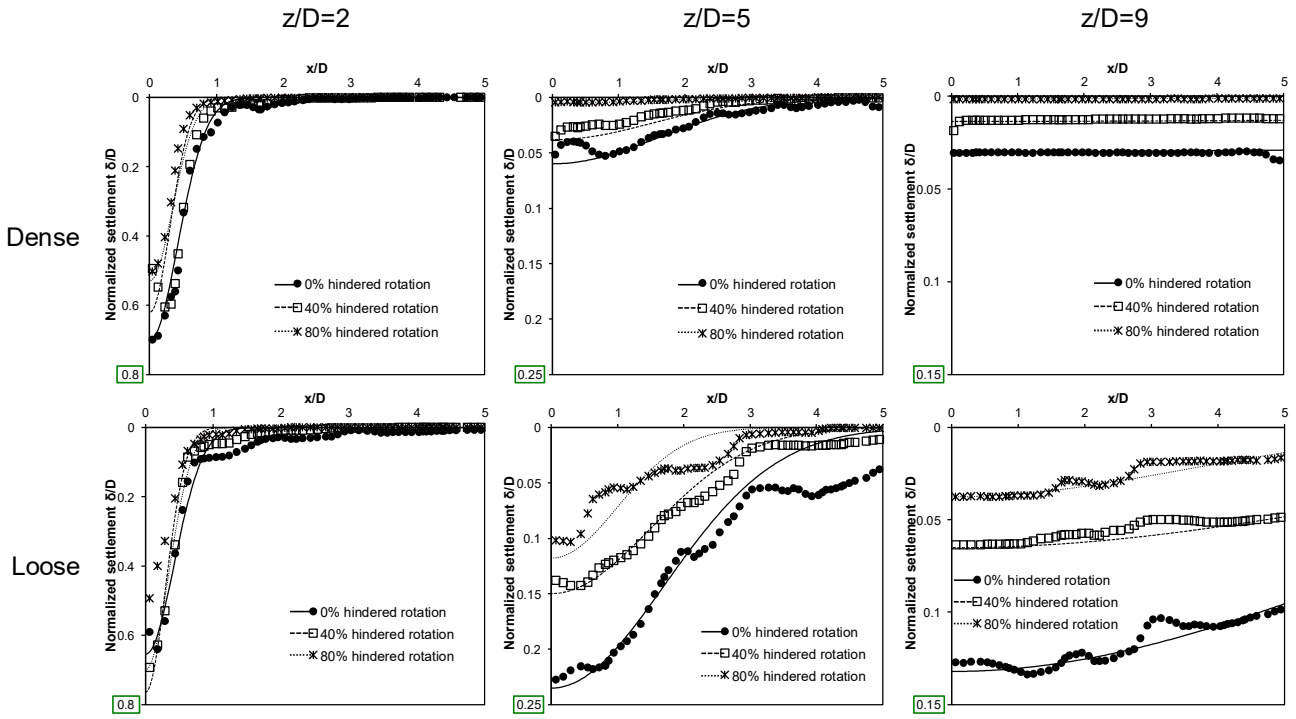

Figure 5. Surface settlement after dissolution. The data—folded at the centerline—are fitted with a Gaussian function. Note the ranges in y-axes are not the same for different z/D as indicated by the green square frames.

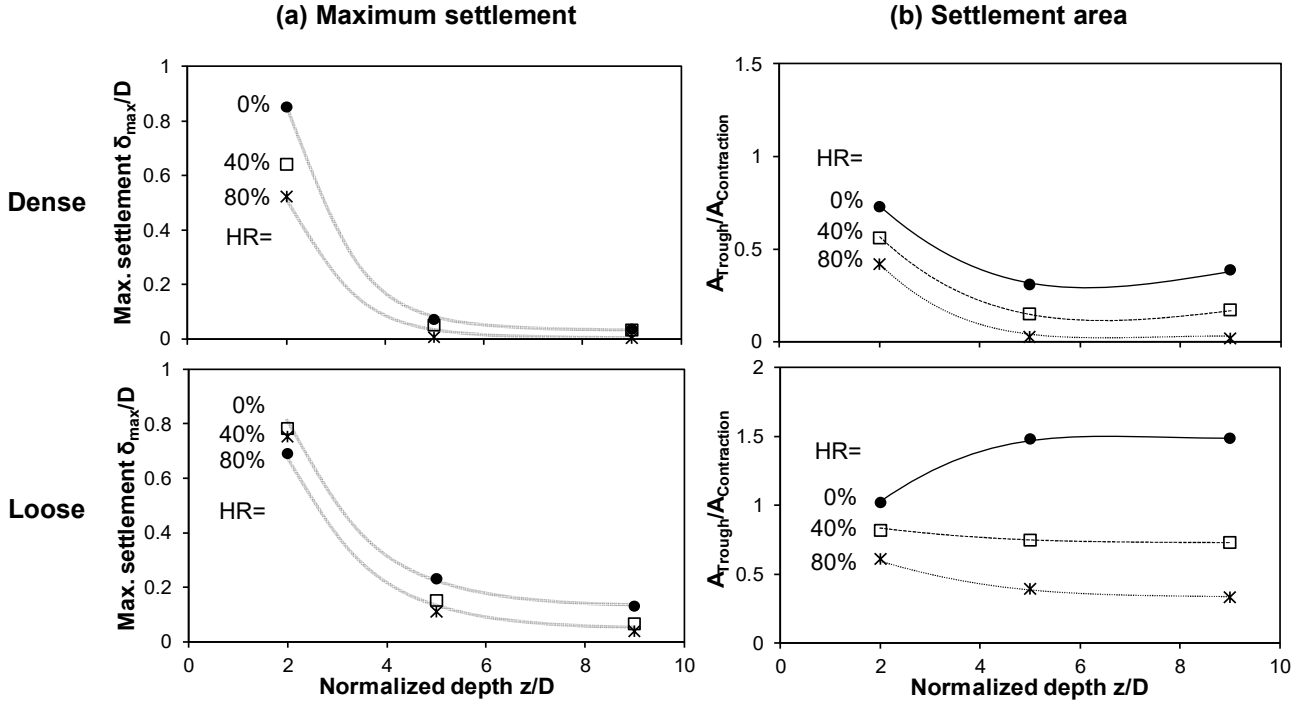

Figure 6. Surface settlement for subsurface cavity dissolution in dense and loose sediments. (**a**) Normalized maximum settlement δ_{max} to inclusion diameter D. (**b**) Trough area A_{tr} normalized by the area of contracting zone A_{cz}.

4. Discussion

Boundary effects. Some surface settlement profiles do not die out within the simulated width. This is a clear indication that simulations are affected by boundary effects (worst

conditions: deep inclusions in loose packings—Figure 5). An alternative view is to consider these simulations as a representative REV that repeats itself with characteristic L-spacing. Similarly, there is some interaction with the lower boundary, particularly in the case of deep inclusions (z/D = 9—see Figures 3 and 4).

Shallow vs. *deep dissolving inclusions.* To explore the dissolution of deep inclusions subjected to constant vertical stress, we conducted a complementary study. (Note: In both cases, the lateral boundary imposes zero lateral deformation; however, inclusion size and sediment density show minor differences) [48]. Deep inclusion is simulated by applying constant vertical stress (e.g., 100 kPa for the case shown in Figure 7) using plate boundary loading from the top and the bottom of the specimen. Both top and bottom boundaries move in as the inclusion contracts.

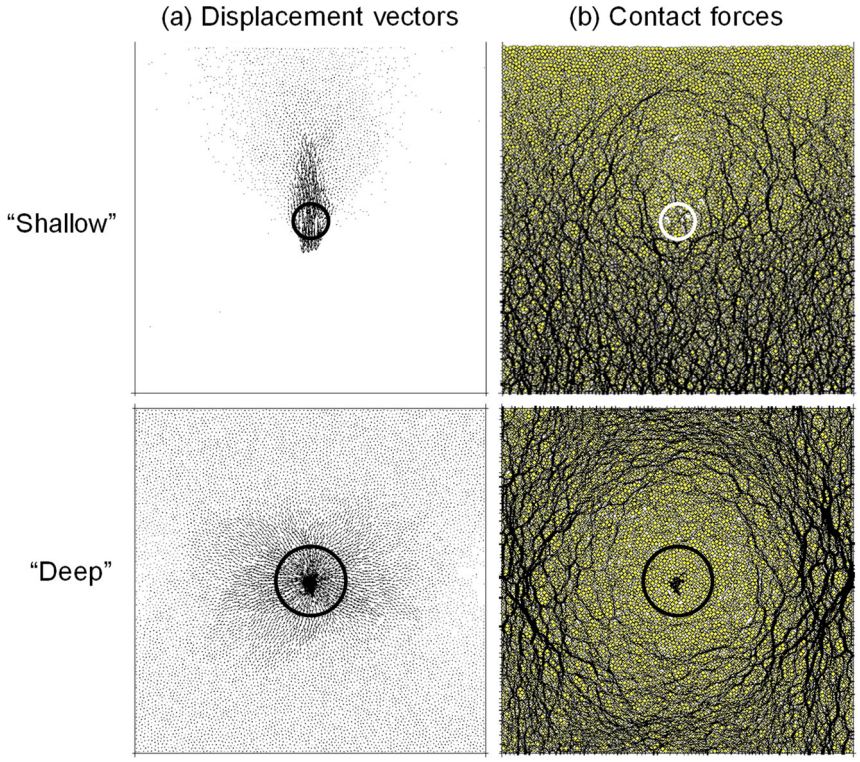

Figure 7. Shallow versus deep volume loss. (**a**) Displacement vectors and (**b**) contact forces after dissolution. The deep inclusion is subjected to constant vertical stress of 100 kPa, and both the top and bottom boundaries move in as the inclusion contracts. The circles show the original size of the contracting zone. Note: HR = 40% in both cases.

The results displayed in Figure 7 highlight distinct differences in granular flow and force arching. In particular, while the prevalent gravity-driven vertical flow occurs when shallow inclusions dissolve, horizontal grain displacement prevails in dissolving deep inclusions. Similarly, while gravity and the stress gradient underly the evolution of force chains in shallow inclusions, concentric arches form when dissolution takes place under constant vertical stress (i.e., when a local change in vertical stress is minor compared to the stress level).

Post-dissolution sediment properties. Local volume contraction affects interparticle forces and porosity in an area that is significantly larger than the initial size of the contracting zone (Figure 4 and Figure S2). Based on published numerical and experimental results, we anticipate a more contractive sediment response to subsequent normal and shear loading, lower undrained strength, and lower shear wave velocity within the "ghost zones" [49–53].

Field implications. Displacements induced by underground volume contraction affect the overlying infrastructure and nearby underground structures. For example, piles experience lateral deflection, bending moments, settlement, and abnormal load distribution [14–16]; lifelines are sheared and disrupted [18–21,54]; buildings develop differential settlements and horizontal displacement [22,23]; and adjacent tunnels may rotate and undergo asymmetric settlement [25,26].

Scaling relations and similarities limit the extrapolation of the numerical results presented here to field conditions where the contracting cavity size is much larger than the grain size, D >> d. Nevertheless, macroscale trends observed in the context of tunnels resemble the results gathered in this study: the settlement volume correlates with the ground loss [55,56], the maximum surface settlement decreases as the soil stiffness increases [57], and volume loss at greater depths causes less surface settlement but a wider settlement trough [45,58].

5. Conclusions

Mineral dissolution and precipitation are concurrent soil processes and can take place in relatively short time scales in advective regimes and when minerals are far from equilibrium. To study the consequences of localized mineral dissolution at shallow depths, that is, free surface conditions, we used a two-dimensional discrete element code.

Grains slide and flow to refill the space left behind by dissolution. There are successive arch formation and collapse events, and a porosity front propagates upwards as grains flow down during refilling. Grains are loosely packed around and within the refilled cavity; the small forces they carry provide transverse support to the egg-shaped granular arches that form around the shallow dissolving zone under gravity. In contrast, granular flow is primarily horizontal in deep dissolving inclusions under constant far field vertical stress, and force arches are concentric around the region that experience mass loss. Published numerical and experimental results suggest that both the shallow and deep sediment will be more contractive and exhibit a lower undrained strength and shear stiffness after dissolution.

Granular rearrangement following dissolution involves particle rotation and sliding. Higher coordination numbers in denser packings and interlocking by hindered rotation combine to exacerbate rotational frustration. Consequently, localized dissolution within denser packings with higher interlocking results in more pronounced force chain arches, looser fill, reduced peak settlement and trough areas, and narrower granular flow streams and settlement troughs.

In most cases, the settlement trough area is smaller than the lost inclusion area. In fact, the overlying sediment can hide the localized dissolution and surface settlement vanishes when deep inclusions ($z/D \geq 5$) dissolve within dense sediments. Dissolution-triggered densification may take place but only in very loose sediments.

While scaling relations and similarity limit the extrapolation of these numerical results to tunneling and mining applications, macroscale trends observed in the field resemble results gathered in this study.

Supplementary Materials: The following supporting information can be downloaded at: https://www.mdpi.com/article/10.3390/app12168015/s1.

Author Contributions: Conceptualization, J.C.S.; software, M.C.; investigation, M.C.; resources, J.C.S.; data curation, M.C.; writing—original draft, M.C.; writing—review and editing, J.C.S.; supervision, J.C.S. All authors have read and agreed to the published version of the manuscript.

Funding: Support for this research was provided by the KAUST endowment and the US Department of Energy Savannah River Operations Office. This research was also supported by Basic Science Research Program through the National Research Foundation of Korea (NRF) funded by the Ministry of Education (2019R1A6A1A10072987).

Institutional Review Board Statement: Not applicable.

Informed Consent Statement: Not applicable.

Data Availability Statement: The data are available from the corresponding author upon reasonable request.

Acknowledgments: Gabrielle E. Abelskamp edited the manuscript.

Conflicts of Interest: On behalf of all authors, the corresponding author states that there is no conflict of interest.

References

1. Gutiérrez, F.; Desir, G.; Gutiérrez, M. Causes of the catastrophic failure of an earth dam built on gypsiferous alluvium and dispersive clays (Altorricón, Huesca Province, NE Spain). *Environ. Geol.* **2003**, *43*, 842–851. [CrossRef]
2. Herrera, M.C.; Lizcano, A.; Santamarina, J.C. (Eds.) *Colombian Volcanic Ash Soils*; Taylor & Francis: Singapore, 2007; pp. 2385–2409.
3. Lee, J.Y.; Santamarina, J.C.; Ruppel, C. Volume change associated with formation and dissociation of hydrate in sediment. *Geochem. Geophys. Geosyst.* **2010**, *11*, Q03007. [CrossRef]
4. Espinoza, D.N.; Kim, S.; Santamarina, J.C. CO_2 geological storage—Geotechnical implications. *KSCE J. Civ. Eng.* **2011**, *15*, 707–719. [CrossRef]
5. Bachus, R.C.; Terzariol, M.; Pasten, C.; Chong, S.H.; Dai, S.; Cha, M.S.; Kim, S.; Jang, J.; Papadopoulos, E.; Roshankhah, S.; et al. Characterization and Engineering Properties of Dry and Ponded Class-F Fly Ash. *J. Geotech. Geoenviron. Eng.* **2019**, *145*, 04019003. [CrossRef]
6. Kim, S.; Espinoza, D.N.; Jung, J.; Cha, M.; Santamarina, J.C. Chapter 17—Carbon Geological Storage: Coupled Processes, Engineering and Monitoring. In *Science of Carbon Storage in Deep Saline Formations*; Newell, P., Ilgen, A.G., Eds.; Elsevier: Amsterdam, The Netherlands, 2019; pp. 383–407.
7. Dold, B. Submarine Tailings Disposal (STD)—A Review. *Minerals* **2014**, *4*, 642–666. [CrossRef]
8. Bell, F.G.; Stacey, T.R.; Genske, D.D. Mining subsidence and its effect on the environment: Some differing examples. *Environ. Geol.* **2000**, *40*, 135–152. [CrossRef]
9. Cui, X.; Miao, X.; Wang, J.a.; Yang, S.; Liu, H.; Song, Y.; Liu, H.; Hu, X. Improved prediction of differential subsidence caused by underground mining. *Int. J. Rock Mech. Min. Sci.* **2000**, *37*, 615–627. [CrossRef]
10. Attewell, P.B.; Farmer, I.W. Ground Deformations Resulting from Shield Tunnelling in London Clay. *Can. Geotech. J.* **1974**, *11*, 380–395. [CrossRef]
11. Wang, G.; Fang, Q.; Du, J.; Yang, X.; Wang, J. Estimating Volume Loss for Shield-Driven Tunnels Based on the Principle of Minimum Total Potential Energy. *Appl. Sci.* **2022**, *12*, 1794. [CrossRef]
12. Li, W. Prediction of surface settlement due to the displacement of soft zones. In Proceedings of the Fourth International Conference on Deformation Characteristics of Geomaterials, Atlanta, GA, USA, 3 March 2008; pp. 413–419.
13. Aljammaz, A.; Sultan, M.; Izadi, M.; Abotalib, A.Z.; Elhebiry, M.S.; Emil, M.K.; Abdelmohsen, K.; Saleh, M.; Becker, R. Land Subsidence Induced by Rapid Urbanization in Arid Environments: A Remote Sensing-Based Investigation. *Remote Sens.* **2021**, *13*, 1109. [CrossRef]
14. Chen, L.T.; Poulos, H.G.; Loganathan, N. Pile responses caused by tunneling. *J. Geotech. Geoenviron. Eng.* **1999**, *125*, 207–215. [CrossRef]
15. Huang, M.S.; Zhang, C.R.; Li, Z. A simplified analysis method for the influence of tunneling on grouped piles. *Tunn. Undergr. Space Technol.* **2009**, *24*, 410–422. [CrossRef]
16. Jacobsz, S.W.; Standing, J.R.; Mair, R.J.; Hagiwara, T.; Sugiyama, T. Centrifuge modelling of tunnelling near driven piles. *Soils Found.* **2004**, *44*, 49–56. [CrossRef]
17. Huang, K.; Sun, Y.; Kuang, X.; Huang, X.; Liu, R.; Wu, Q. Study on the Restraint Effect of Isolation Pile on Surface Settlement Trough Induced by Shield Tunnelling. *Appl. Sci.* **2022**, *12*, 4845. [CrossRef]
18. Vorster, T.E.B.; Klar, A.; Soga, K.; Mair, R.J. Estimating the effects of tunneling on existing pipelines. *J. Geotech. Geoenviron. Eng.* **2005**, *131*, 1399–1410. [CrossRef]
19. Klar, A.; Marshall, A.M.; Soga, K.; Mair, R.J. Tunneling effects on jointed pipelines. *Can. Geotech. J.* **2008**, *45*, 131–139. [CrossRef]
20. Marshall, A.M.; Klar, A.; Mair, R.J. Tunneling beneath Buried Pipes: View of Soil Strain and Its Effect on Pipeline Behavior. *J. Geotech. Geoenviron. Eng.* **2010**, *136*, 1664–1672. [CrossRef]
21. Wang, Y.; Shi, J.W.; Ng, C.W.W. Numerical modeling of tunneling effect on buried pipelines. *Can. Geotech. J.* **2011**, *48*, 1125–1137. [CrossRef]
22. Yoo, C.; Kim, J.-H. A web-based tunneling-induced building/utility damage assessment system: TURISK. *Tunn. Undergr. Space Technol.* **2003**, *18*, 497–511. [CrossRef]
23. Burland, J.B.; Standing, J.R.; Jardine, F.M. Assessing the risk of building damage due to tunnelling—Lessons from the Jubilee Line Extension, London. In Proceedings of the 14th Southeast Asian Geotechnical Conference, Hong Kong, China, 10–14 December 2001; pp. 17–44.
24. Providakis, S.; Rogers, C.D.F.; Chapman, D.N. Assessing the Economic Risk of Building Damage due to the Tunneling-Induced Settlement Using Monte Carlo Simulations and BIM. *Sustainability* **2020**, *12*, 10034. [CrossRef]

25. Cooper, M.L.; Chapman, D.N.; Chan, A.H.C.; Rogers, C.D.F. Tunnel-induced ground movements and their effects on existing tunnels. In Proceedings of the Fifteenth International Conference on Soil Mechanics and Geotechnical Engineering, Istanbul, Turkey, 27 August 2001; Volumes 1–3; pp. 1483–1486.
26. Cooper, M.L.; Chapman, D.N.; Rogers, C.D.F.; Chan, A.H.C. Movements in the Piccadilly Line tunnels due to the Heathrow Express construction. *Geotechnique* **2002**, *52*, 243–257. [CrossRef]
27. Zheng, B.; Elsworth, D. Evolution of permeability in heterogeneous granular aggregates during chemical compaction: Granular mechanics models. *J. Geophys. Res. Solid Earth* **2012**, *117*. [CrossRef]
28. Cha, M.; Santamarina, J.C. Pressure-dependent grain dissolution using discrete element simulations. *Granul. Matter* **2019**, *21*, 101. [CrossRef]
29. Bista, H.; Panthi, S.; Hu, L. Chemo-Mechanical Couplings at Granular Contact: The Effect of Mineral Dissolution and Precipitation across the Scales. *Geotechnics* **2022**, *2*, 158–170. [CrossRef]
30. Cha, M.; Santamarina, J.C. Dissolution of randomly distributed soluble grains: Post dissolution k_0-loading and shear. *Géotechnique* **2014**, *64*, 828–836. [CrossRef]
31. Bym, T.; Marketos, G.; Burland, J.; O'sullivan, C. Use of a two-dimensional discrete-element line-sink model to gain insight into tunnelling-induced deformations. *Géotechnique* **2013**, *63*, 791. [CrossRef]
32. Marshall, A.M.; Elkayam, I.; Klar, A. Ground behaviour above tunnels in sand-DEM simulations versus centrifuge test results. In Proceedings of the Euro: Tun 2009, 2nd International Conference on Computational Methods in Tunnelling, Bochum, Germany, 9–11 September 2009; pp. 9–11.
33. Itasca Consulting Group. *PFC2D Users' Manual (Version 3.1)*; Itasca Consulting Group: Minneapolis, MN, USA, 2004.
34. O'Sullivan, C. *Particulate Discrete Element Modelling: A Geomechanics Perspective*; Taylor & Francis: New York, NY, USA, 2011.
35. Mohamed, A.; Gutierrez, M. Comprehensive study of the effects of rolling resistance on the stress-strain and strain localization behavior of granular materials. *Granul. Matter* **2010**, *12*, 527–541. [CrossRef]
36. Fukumoto, Y.; Sakaguchi, H.; Murakami, A. The role of rolling friction in granular packing. *Granul. Matter* **2013**, *15*, 175–182. [CrossRef]
37. Iwashita, K.; Oda, M. Rolling resistance at contacts in simulation of shear band development by DEM. *J. Eng. Mech.-ASCE* **1998**, *124*, 285–292. [CrossRef]
38. Jiang, M.; Shen, Z.; Wang, J. A novel three-dimensional contact model for granulates incorporating rolling and twisting resistances. *Comput. Geotech.* **2015**, *65*, 147–163. [CrossRef]
39. Lu, M.; McDowell, G. The importance of modelling ballast particle shape in the discrete element method. *Granul. Matter* **2007**, *9*, 69–80. [CrossRef]
40. Guises, R.; Xiang, J.; Latham, J.-P.; Munjiza, A. Granular packing: Numerical simulation and the characterisation of the effect of particle shape. *Granul. Matter* **2009**, *11*, 281–292. [CrossRef]
41. Wang, J.; Yu, H.S.; Langston, P.; Fraige, F. Particle shape effects in discrete element modelling of cohesive angular particles. *Granul. Matter* **2011**, *13*, 1–12. [CrossRef]
42. Bardet, J.P. Observations on the effects of particle rotations on the failure of idealized granular materials. *Mech. Mater.* **1994**, *18*, 159–182. [CrossRef]
43. Suiker, A.S.J.; Fleck, N.A. Frictional Collapse of Granular Assemblies. *J. Appl. Mech.* **2004**, *71*, 350–358. [CrossRef]
44. Cha, M.; Santamarina, J.C. Effect of dissolution on the load–settlement behavior of shallow foundations. *Can. Geotech. J.* **2016**, *53*, 1353–1357. [CrossRef]
45. Peck, R.B. Deep Excavations and Tunneling in Soft Ground. In Proceedings of the 7th International Conference on Soil Mechanics and Foundation Engineering, Mexico City, Mexico, 29 August 1969; pp. 225–290.
46. Mair, R.J.; Taylor, R.N.; Bracegirdle, A. Subsurface settlement profiles above tunnels in clays. *Geotechnique* **1993**, *43*, 315–320. [CrossRef]
47. Fang, Y.S.; Lin, J.S.; Su, C.S. An estimation of ground settlement due to shield tunneling by the Peck-Fujita method. *Can. Geotech. J.* **1994**, *31*, 431–443. [CrossRef]
48. Cha, M.; Santamarina, J.C. Localized dissolution in sediments under stress. *Granul. Matter* **2019**, *21*, 79. [CrossRef]
49. Cha, M.; Santamarina, J.C. Predissolution and Postdissolution Penetration Resistance. *J. Geotech. Geoenviron. Eng.* **2013**, *139*, 2193–2200. [CrossRef]
50. Tran, M.K.; Shin, H.; Byun, Y.-H.; Lee, J.-S. Mineral dissolution effects on mechanical strength. *Eng. Geol.* **2012**, *125*, 26–34. [CrossRef]
51. Fam, M.A.; Cascante, G.; Dusseault, M.B. Large and small strain properties of sands subjected to local void increase. *J. Geotech. Geoenviron. Eng.* **2002**, *128*, 1018–1025. [CrossRef]
52. Truong, Q.H.; Eom, Y.H.; Lee, J.S. Stiffness characteristics of soluble mixtures. *Géotechnique* **2010**, *60*, 293–297. [CrossRef]
53. Cha, M.; Santamarina, J.C. Hydro-chemo-mechanical coupling in sediments: Localized mineral dissolution. *Geomech. Energy Environ.* **2016**, *7*, 1–9. [CrossRef]
54. Klar, A.; Vorster, T.E.B.; Soga, K.; Mair, R.J. Soil-pipe interaction due to tunnelling: Comparison between Winkler and elastic continuum solutions. *Geotechnique* **2005**, *55*, 461–466. [CrossRef]
55. Rowe, R.K.; Lo, K.Y.; Kack, G.J. A method of estimating surface settlement above tunnels constructed in soft ground. *Can. Geotech. J.* **1983**, *20*, 11–22. [CrossRef]

56. Lee, K.M.; Rowe, R.K.; Lo, K.Y. Subsidence owing to tunnelling. I. Estimating the gap parameter. *Can. Geotech. J.* **1992**, *29*, 929–940. [CrossRef]
57. Bobet, A. Analytical solutions for shallow tunnels in saturated ground. *J. Eng. Mech.-ASCE* **2001**, *127*, 1258–1266. [CrossRef]
58. Ahmed, M.; Iskander, M. Analysis of Tunneling-Induced Ground Movements Using Transparent Soil Models. *J. Geotech. Geoenviron. Eng.* **2011**, *137*, 525–535. [CrossRef]